24th INTERNATIONAL CONGRESS ON SOUND AND VIBRATION
23–27 July 2017, London

ICSV24
23-27JULY 2017
LONDON CALLING

# IDENTIFICATION OF FLAME DISPLACEMENT FROM HIGH FREQUENCY THERMOACOUSTIC PULSATIONS IN GAS TURBINE COMBUSTORS

Frederik M. Berger[1], Jan Kaufmann[1], Bruno Schuermans[2], Thomas Sattelmayer[1]
[1] *Lehrstuhl für Thermodynamik, Technische Universität München, Germany*
[2] *GE Power, Switzerland*
*email: berger@td.mw.tum.de*

Non-compact thermoacoustic pulsations at screech level frequencies are observed in a can-type combustor, which reveal a transverse flame displacement as a driving mechanism. This flame displacement effect is studied via an identification routine to evaluate the oscillatory displacement field from highly time resolved flame $OH^\star$ chemiluminescence recordings. Phase conditioned averaging of the resulting data allows to reconstruct the acoustic oscillation cycle. With this evaluation routine, the resulting heat release modulation can be identified with simple and robust measurement techniques. These flame displacement fields are compared against respective fields from synchronous acoustic PIV measurements to assess the method's applicability. The results show the spatially variable displacement field and its dependence on the acoustic pressure amplitude and phase. Ultimately, the findings of this study allow to decompose the total heat release modulation field obtained from experimental data (available from previous works) into its individual contributions, which are local heat release modulations via the acoustic displacement and density.

Keywords: High-Frequency Thermoacoustics, Non-Compact Systems, Screech, Flame Displacement

## 1. Introduction

Lean premixed combustion technology optimizes the efficiency of modern power generating gas turbines towards reduced emission levels, flexible operability and economic competitiveness. However, a major engineering challenge for such combustion systems is their high tendency towards self-sustained thermoacoustic instabilities. These instabilities are the result of the constructive interference of resonant acoustic pressure pulsations in the combustion chamber with the heat release. Their occurrence hampers a smooth engine operation or even leads to severe hardware damage. Thermoacoustic pulsations appear at different oscillation frequencies and acoustic modes for various operation conditions. Due to these factors, the implementation of mitigation techniques are required to ensure a flexible engine operation, often at the compromise of overall efficiency. Therefore, physical understanding of flame-acoustic feedback mechanisms is essential to develop effective design strategies to improve the engine's thermoacoustic stability.

This work contributes to the identification of non-compact flame response mechanisms, as observed in high-frequency (HF), transverse thermoacoustic oscillations. The understanding and mitigation techniques of longitudinal, low-frequency (LF) instabilities are well advanced, while HF instabilities are less explored and have been receiving increased attention only recently. The main difference between HF and LF thermoacoustics is the characteristic flame-acoustic length scales. These are in the same order of magnitude for HF systems and render the flame non-compact [1]. In other words, local in-phase interactions of flame-acoustics dominate in HF systems over convective/time-lag characterized flame modulations, observed in LF systems. This results in a locally varying modulation of the flame. It was shown previously that these modulations result in flame driving by a periodic flame displacement and deformation in-phase with the pressure field [2, 3].

In this study, the acoustically induced flame displacement is experimentally quantified for the first time by cross-correlating instantaneous flame images. Furthermore, the local acoustic pressure is recorded simultaneously to the flame information for a phase-dependent evaluation. With this processing method, the spatially and temporally variable flame displacement can be visualized by a vector field, and thereby allows to reconstruct the resulting heat release oscillation image only governed by the flame motion. This approach is methodically comparable to the reconstruction of the acoustic velocity field with conditional particle image velocimetry (PIV) [4, 5]. Hence, reconstructed flame modulation fields are compared equivalent fields based on PIV measurements to assess its accuracy. Conclusively, this new method is applied to flame images of a high frequency thermoacoustically unstable model combustor for the analysis of pulsation amplitude-dependent displacement behavior. With this, a pure experimental visualization of non-compact thermoacoustic source term distributions is now possible, which ultimately improves the understanding of screech in gas turbines.

## 2. Swirl-Stabilized Combustor Experiment

The experimental setup is a generic lean premixed gas turbine combustor with a can type chamber operated at atmospheric conditions. A schematic of the setup including diagnostic equipment is given in Fig. 1(a).

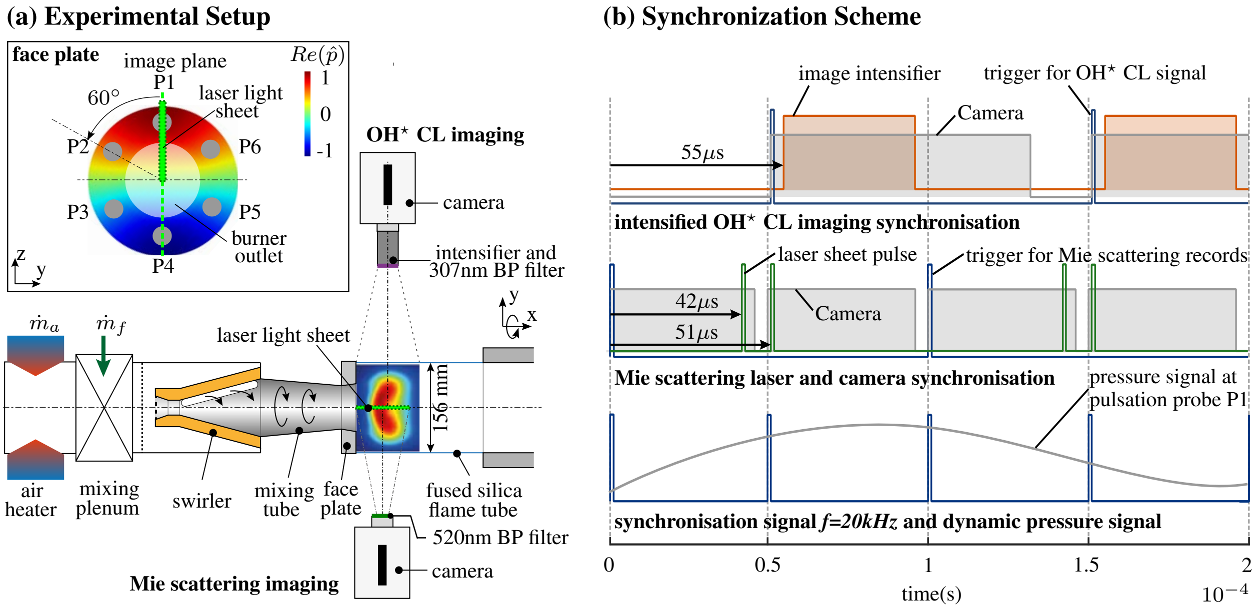

Figure 1: (a) Schematic of the experimental setup with OH*CL and Mie scattering imaging units, and instrumentation ports for pressure measurements. (b) Synchronization scheme for acoustic pressure phase resolved OH*CL and Mie scattering imaging.

Following the setup in the mean fluid flow direction, incoming air is first preheated to $T = 473K$ and premixed with natural gas fuel. A cone shaped swirler induces an adjustable tangential momentum to the flow. After passing a mixing section, the perfectly premixed fuel-air mixture is released into the quartz glass flame tube, in which flame stabilization occurs through inner and outer recirculation of the swirling flow. The flame tube is extended by an open end exhaust duct with equal diameter and approximately $2m$ length. A detailed description of the experiment and discussion of the resulting flow and flame characteristics are given in [2, 6].

## 3. Data Acquisition and Investigation of HF Thermoacoustic Pulsations

At certain operation conditions, the burner configuration exhibits a self-excited thermoacoustic instability of the first transverse mode, which oscillates at a frequency $f_{T1} \approx 3,000Hz$. Samples of the pressure measurement at the combustor face plate, as well as the flame heat release (indicated by OH*Cl intensity) fluctuations are given in Fig. 2 (a-c). Recently, the underlying physical flame feedback mechanisms and modelling strategies of the observed instability have been investigated in [1, 2, 3]. One key result of these works is the identification of non-compact flame response mechanisms that describe the heat release modulation via the local feedback to the acoustic pressure oscillations. These response mechanisms are identified and formulated by a periodic flame displacement $q'_\Delta$ and flame deformation $q'_\rho$ in-phase with the acoustic pressure. Analytical source terms

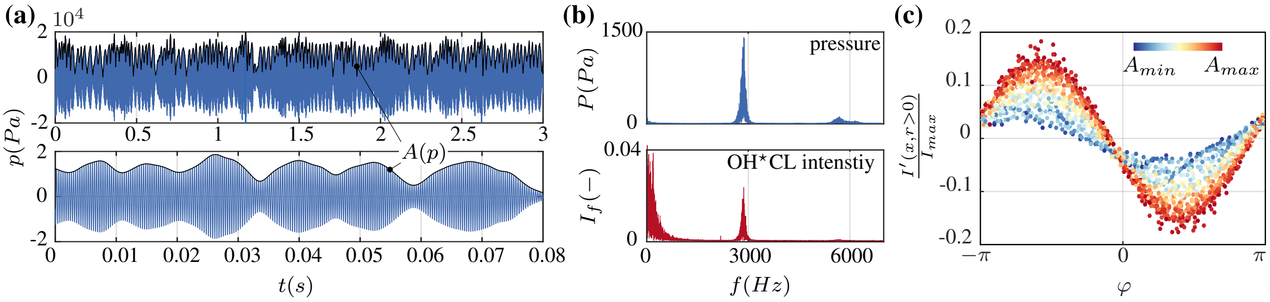

Figure 2: (a) Sample pressure time trace, (b) frequency profile of the pressure and heat-release oscillations, and (c) flame-chemiluminescence intensity oscillations from OH*CL recordings (intensity fluctuation integrated in $(x, r > 0)$) over the pressure phase measured at face plate position P1, color coded with respective pressure envelope amplitude.

were determined and validated against experimentally obtained counterparts. In the present study, the identification framework is extended by the measurement of the flame displacement with the acoustic gradient - i.e. $q'_\Delta$ is isolated from $q'$. This allows to visualize and cross-validate the individual ($q'_\Delta$ and $q'_\rho$) non-compact flame response from experimental data against analytical models, which has not been possible before [2].

The experimental identification of the pure flame displacement field relies on cross-correlating two subsequent flame recordings. The employed method comprises the extraction of the displacement field from line-of-sight integrated OH* CL images. However, a correlation of chemical reaction rate chemiluminescence recordings with an acoustic flame displacement is non-intuitive. Therefore, in the following discussion, line-of-sight integrated OH* CL based heat release fields by flame displacement are compared to counterparts obtained from simultaneously recorded acoustic PIV images. The related PIV displacement fields are retrieved from planar laser-light flow-particle scattering measurements. These reference fields are then used to verify the routines validity.

For this quantitative identification of the acoustically induced flame motion from OH*CL and PIV recordings, simultaneous measurements are conducted for:

1. The line-of-sight integrated OH*CL signal via the flame chemiluminescence bandpass filtered at $\lambda = 307 \pm 10nm$,
2. the Mie scattering of the reacting flow mixed with $TiO_2$ particles from a thin laser light sheet through the burner center line (detailed setup description in [7]), and
3. the dynamic pressure oscillations at the burner face plate,

as indicated in Fig. 1 (a) and (b). Image recordings were conducted with high-speed CMOS cameras at imaging frequencies of $f_s = 10,000$ and $20,000$ frames/s for the OH*CL and Mie scattering recordings, respectively. Accordingly, the PIV laser pulse frequency is also at $20,000$ pulses/s. Recording times per sequence are $2.4s$. Such high repetition rates are necessary to obtain a phase-dependent resolution of the $3000Hz$ flame oscillation. The synchronization is implemented with a master clock signal, as shown in Fig. 1 (b). This figure also shows the synchronization strategy, the shutter/pulse times of the individual measurement systems, and a sample pressure signal for phase-conditioned image evaluation. The following section describes the image processing that is applied, and is followed by the presentation of the results, as well as a comparison against computed acoustic flame displacement fields from analytic models.

## 4. Reconstruction of Acoustically Induced Flame Displacement

The starting point for this analysis is the observation that the recorded line-of-sight integrated OH*CL intensity field of an unstable operation point shows a distinct transverse, oscillatory/rotating motion. The oscillation frequency is equal to the measured dynamic pressure frequency (Fig. 2 (b,c)). In order to comprehensively characterize the displacement effect on flame driving, the local displacement magnitude, pulsation amplitude dependence, and spatial distribution are important. For the following discussion, two main discrepancies between acoustic PIV and the herein introduced method need to be taken into account: First, the measured quantity is the displacement of the flame reaction zone that does not necessarily coincide with the acoustic velocity magnitude. Second, instantaneous line-of-sight integrated OH$^\star$CL fields are processed instead of planar cut-plane data from laser measurements. The latter introduces a systematic measurement error, which is assessed in the results section. Instead of tracking a tracer particle pattern, as utilized in PIV methods [4, 5, 8], the basis for the displacement field reconstruction is the local deformation of the recorded time-variate flame structure - i.e. the local flame intensity distribution. This approach is schematically shown in Fig. 3. The following paragraphs show the OH$^\star$CL image processing and reconstruction procedure. Handling of the Mie scattering images and PIV postprocessing for reference fields is not discussed due to the availability of detailed reports in the literature e.g. [4, 5, 7, 8].

## 4.1 Image Pre-Processing

The bandpass filtered recording of the combustion process $I((x),t)$ at the time instance $t$ shows the instantaneous line-of-sight integrated flame chemiluminescence signal accompanied by noise from the image intensification (Fig. 3 (a) - raw image). In order to improve the efficiency of the following displacement-field reconstruction, the image contrast is enhanced followed by smoothing of the raw image. Contrast enhancement is applied via contrast-limited adaptive histogram equalization (CLAHE), which optimizes the flame displacement identification in areas of low signal intensity. As only the acoustically induced motion of the flame brush is of interest, the resulting image is smoothed to accentuate the global flame structure instead of local intensity peaks (Fig. 3 (a) - smoothed image). Afterwards, the images are divided into uniform interrogation windows $W$ (sub-images), shown in Fig. 3 (b). Each of these window yields one displacement vector and thereby allows for a spatial resolution of the flame displacement. The window size is optimized for a high displacement field resolution, while maintaining a sufficient data basis for the reconstruction of the local displacement vector.

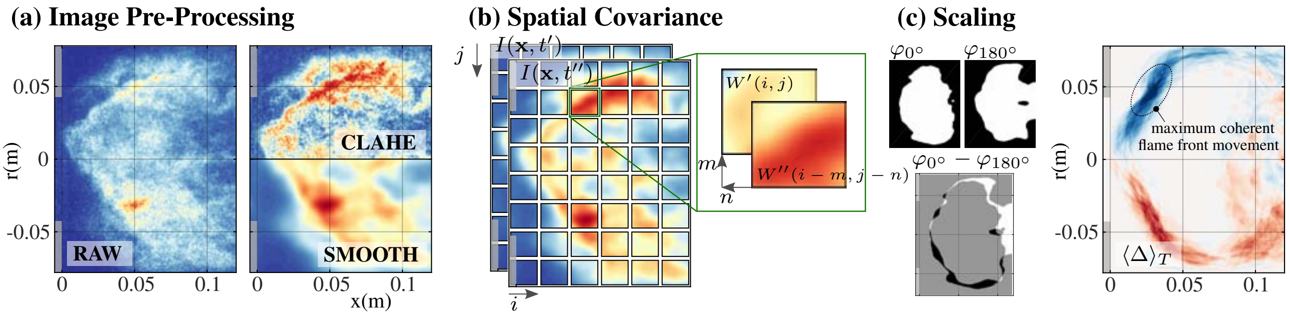
**(a) Image Pre-Processing** **(b) Spatial Covariance** **(c) Scaling**

Figure 3: (a) Pre-processing of the raw image, (b) cross-correlation of two subsequent flame images with indication of windowing, (c) evaluation of a scaling factor for the peak displacement from the mean field of difference images of the binarized flame structure $\langle\Delta\rangle_T$ at phase positions $\varphi = 0°, 180°$.

## 4.2 Spatial Covariance of Subsequent Flame Images

The spatial covariance of two subsequent OH$^\star$CL images $I(\mathbf{x},t')$ and $I(\mathbf{x},t'')$ recorded with a sufficiently short time lag $t_r = t'' - t' = \frac{1}{f_s}$ is evaluated by obtaining the correlation matrix

$$\mathcal{C}(m,n) = \sum_i \sum_j W'(i,j)W''(i-m,j-n) \tag{1}$$

for each window pair $W'(i,j)$ and $W''(i,j)$, where $i,j$ are the window- and $m,n$ the correlation-coordinates. The cross-correlation function in Eq. 1 is a statistical approach that evaluates the pattern matching in the window pair [9, 10]. A displacement of $W'$ towards $W''$ with the highest probable pattern agreement yields a peak in the correlation matrix. This peak is located and then transformed into a distance. The correlation function is applied to all windows of the image pair to obtain a displacement vector field $D(\mathbf{x})$. The evaluation procedure is then repeated for all consecutive image pairs of the recording sequence in order to obtain a time series of instantaneous flame displacement fields $D(\mathbf{x},t)$.

At this point, it is important to note that the spatial covariance field evaluation of an image pair yields a vector field, which depends on (i) the local heat release intensity of the turbulent flame brush, (ii) the flame motion impacted by the mean fluid flow, (iii) the transverse flame motion with the acoustic oscillation, as well as (iv) systematic errors associated with applying the correlation function [10].

### 4.3 Phase-Conditioned Evaluation

In order to extract only the acoustically induced periodic flame motion, mean displacement fields are calculated from (i) the entire time span $\langle D \rangle_T$, and (i) ensembles of images $\langle D \rangle_{\varphi_n}$ corresponding to the same acoustic phase signal $\varphi_n$ within a chosen bin width[1] $\varphi'' - \varphi'$. The phase signal is obtained from the synchronous recordings of the dynamic pressure (Fig. 2 (a)) at the face plate location P1 (Fig. 1 (a)). Bandpass filtering around the dominant transverse oscillation frequency $f_{T1}$ and polar decomposing of the time series yields a complex signal representation containing the relative phase information [2]. A mismatch between recording frequency and oscillation frequency of the thermoacoustic instability, as well as a sufficient sample number $N$ allows to gain an ensemble of flame images - and thus displacement fields - within each phase bin throughout the oscillation cycle. In order to extract only the oscillating information of the displacement field at the specific phase condition, the mean contribution is subtracted from each ensemble average $\langle D \rangle_{\varphi_n} - \langle D \rangle_T$.

### 4.4 Reconstruction of the Oscillatory Displacement Field

The previously obtained phase locked displacement fields contain the information of the flame motion starting within a phase bin $\varphi_n$ for the time lag between recording of the subsequent images $t_r$. This makes it necessary to consider that different time lags result, depending on the time resolution of either $t_\varphi = \frac{1}{f_{T1} N_\varphi}$ or $t_r$. In the presented case, $t_r$ exceeds $t_\varphi$. As the quantity and field of oscillatory displacement is of interest, calculation of the displacement magnitude requires a scaling with the time lag within each phase bin

$$\langle \tilde{D} \rangle_{\varphi_n} = \frac{\langle D \rangle_{\varphi_n}}{t_r f_{T1} N_\varphi}, \tag{2}$$

where $N_\varphi$ is the number of phase intervals. In the next step, the phase resolved flame displacement can be transformed to a complex-denoted representation

$$\mathcal{D}(\mathbf{x}, \varphi) = \frac{1}{N_\varphi} \sum_{n=1}^{N_\varphi} \langle \tilde{D} \rangle_{\varphi_n}(\mathbf{x}) \cdot e^{i\varphi_n}, \tag{3}$$

from the individual phase-locked fields $\langle \tilde{D} \rangle_{\varphi_n}(\mathbf{x})$ related to the phase bin $\varphi_n$, which then describes the spatial flame motion for the entire oscillation cycle.

### 4.5 Scaling of Flame Displacement Magnitude

The above introduced steps for the flame displacement evaluation are appropriate for identification of a qualitative displacement field. However, the introduction of systematic errors complicates a quantitative analysis and results in an underestimation of the displacement magnitude. Errors mainly result from (i) the evaluation of line-of-sight integrated OH$^\star$CL images to retrieve planar information of the acoustically induced displacement (ii) phase-conditioned averaging and (iii) the stochastic/turbulent flame (intensity) dynamics. Hence, the retrieved flame displacement fields $\mathcal{D}(\mathbf{x}, \varphi)$ can be used to indicate the most probable direction of flame motion (in $x, r$ coordinates), but not the local quantitative flame displacement magnitude. In order to quantitatively reproduce the flame motion, instantaneous flame images at phase positions $\varphi = 0^\circ$ and $180^\circ$ are used to identify the maximum transversal displacement of the flame front (Fig. 3 (c)). For this, two flame images consecutively taken at $0^\circ$ and $180^\circ$ are binarized to extract only the global flame front. Afterwards, a difference image of the two former masks is calculated. Averaging a number of these difference images over the recording sequence delivers the maximum oscillatory flame motion $\langle \Delta \rangle_T$, as shown on the right in Fig. 3 (c). From this, a scaling factor is extracted from the marked area close to the outer recirculation zone. This factor is the sum of the local absolute displacement and this specific area is chosen as it is of inherent interest for later identification of the flame/heat release modulation. The constant proportionality factor is then applied for calibration of $\mathcal{D}(\mathbf{x}, \varphi)$, so that the locally extracted magnitude is conserved in a quantitatively correct manner in the displacement field.

---

[1] The bin width specifies the phase resolution for the post-processing procedure and is dependent on the required quality in terms of signal-to-noise ratio of the ensemble-average image.

### 4.6 Reconstruction of the Heat Release Modulation Induced by Flame Displacement

The conclusive step towards the visualization of the pulsating heat release field induced by the flame motion is the transformation of the mean heat release with the displacement field as indicated in Fig. 4 (a).

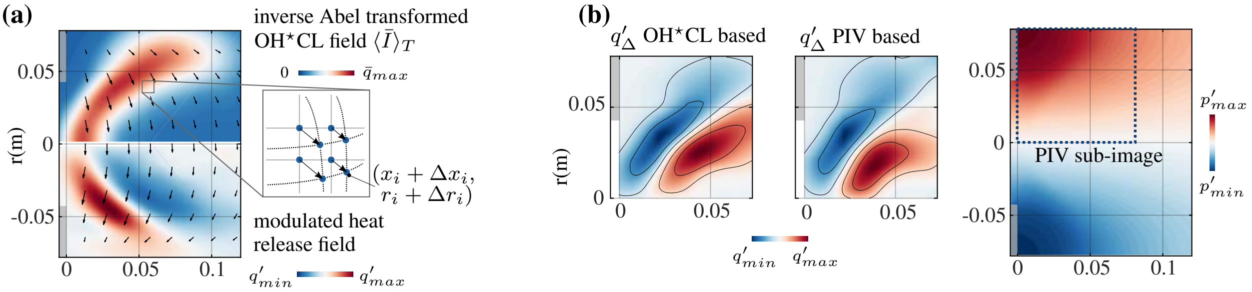

Figure 4: (a) Evaluation of the oscillating heat release field from the displacement result and inverse Abel transformed flame image, (b) resulting heat release oscillations from OH*CL and acoustic PIV data with corresponding pressure field (taken from [2]).

Starting point for identification of the modulated heat release is the time averaged inverse Abel transformed flame image (representing the mean heat release field [2]), and the previously obtained displacement field. Note that the local heat release oscillation phenomenologically results from the acoustically induced transverse motion of the flame brush off its mean position. To reconstruct this oscillating field from the experimental measurements, the coarse displacement field $\mathcal{D}(\mathbf{x}, \varphi)$ is interpolated to a grid that matches the resolution of the heat release map from the OH*CL measurements. The displacement at the wall is set to zero to represent a no-slip wall condition. Afterwards, the $x$ and $r$ coordinates of each pixel in the mean heat release field are deformed in accordance to the local displacement field (schematic in Fig. 4 (a)). This results in a representation of the superposed mean and oscillating heat release field at a certain phase condition. In a final step, the heat release information from the deformed mesh is interpolated back to the original grid and the mean heat release field is subtracted (Fig. 4 (a), lower image half). As a result, the oscillating heat release induced by the displacement effect is visualized in the cut-plane through the burner axis.

## 5. Results

The following section compares the heat release oscillation fields obtained from OH*CL and acoustic PIV measurements. Furthermore, an evaluation of the acoustically induced flame motion and the resulting heat release modulations throughout the oscillation cycle is presented. Finally, the decomposed heat release oscillation fields are shown with reference to the total heat release oscillations, and are compared to numerically computed fields from analytical models.

### 5.1 Comparison of Resulting Heat Release Fields

First, the modulated heat release fields identified from the correlation of subsequent OH*CL images are compared to corresponding fields from acoustic PIV measurements. Note that due to measurement constrains of the setup, as outlined in [7], only a small sub-image is recorded for the acoustic PIV evaluation. Resulting heat release fields are depicted in Fig. 4(b). It can be seen that the principal structure is conserved with both measurement methods. Deviances occur mainly at the downstream position at the inner shear layer zone. These can be attributed to the misleading information from correlating line-of-sight integrated, unsteady flame chemiluminescence data associated with OH*CL images. However, taking the transverse pressure field into account for flame-acoustic interaction, this specific area looses importance because local pressure fluctuations are low. The heat release oscillations occurring in the vicinity of the outer recirculation zone towards the face plate are nearly equal to those obtained from acoustic PIV measurements. These regions are of inherent interest as high pressure pulsation intensities, and thereby strong flame-acoustic interaction are observed here. In the following, the displacement effect on the heat release is further analyzed.

### 5.2 Analysis of Non-Compact Thermoacoustic Source Term Fields

Starting with a general observation, Fig. 5 (a) shows the overall line-of-sight integrated heat release oscillations retrieved from phase-locked averaged OH$^\star$CL images, superposed with the identified flame motion at different phase angles $\varphi$. For optimal visualization of the field distributions, the velocity component is shown instead of the displacement vector, which is linked by $\mathbf{u}' = \partial\Delta'/\partial t$ and results in a 90° phase shift.

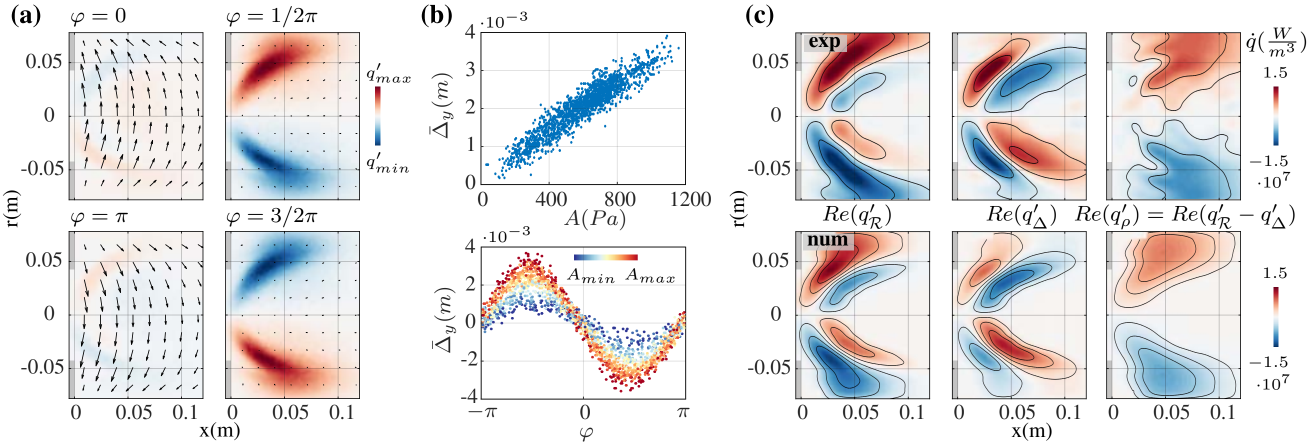

Figure 5: (a) Oscillation cycle of the line-of-sight integrated heat release and displacement, (b) displacement amplitude and oscillation magnitude compared to the acoustic pressure from face plate location P1, (c) tomographic reconstruction and decomposed heat release oscillation fields from experiment and numerical computation (tomographic reconstruction and numerical results taken from [2]).

From this oscillation cycle, it can be seen that the flame moves off its mean position towards the high acoustic pressure region and the displacement is in-phase with the acoustic pressure. Furthermore, the spatial variability of the displacement is observable. Hence, the pulsations of the heat release locally interact with the acoustic pressure and drive the acoustic field with high local heat release oscillation intensity in-phase with high pressure amplitudes. Furthermore, the underling field of the overall oscillating heat release indicates the regions of interest for analyzing the flame-acoustic interaction - i.e. the locations at which the mean flame is modulated by the acoustic fluctuations. Hence, the identified displacement in regions of low heat release intensity are negligible for the analysis as there is no contribution to the total driving. This supports the applicability of the herein introduced method for a simple flame displacement evaluation from OH$^\star$CL compared to more extensive acoustic PIV approaches, as regions where the displacement is identified with a certain error due to the line-of-sight integrated data are occurring mainly towards the pressure node (center of the image). In contrast to this, the displacement of the flame front in the vicinity of the face plate towards the pressure antinode is identified with good confidence.

Next, the amplitude dependence of the displacement effect is studied. The pressure signal at the face plate (Fig. 2 (a)) shows a significant amplitude modulation (beating), which might have an impact on the driving saturation. In order to assess such phenomena, the flame displacement is evaluated in r-direction for each time step in a small sub-image covering the flame front. From this, the oscillations and magnitude of the flame displacement can be correlated with the pressure amplitude and phase shown in Fig. 5 (b). Two distinct features are observable, which are (i) a linear proportionality of the r-displacement magnitude to the pressure amplitude modulation, as well as (ii) the characteristic oscillatory motion of the displacement as already observed for the overall heat release oscillations in Fig. 2 (c).

In a final step, it is possible to decompose the different flame modulation mechanisms, taking also into account the overall heat release modulations gained from tomographic reconstructions of the flame CL. This analysis is carried out for a data set presented in a previous study [2] on non-compact thermoacoustic source terms. A key result from this study is a tomographic reconstruction of the oscillating heat release field $Re(q'_{\mathcal{R}}(\mathbf{x},\varphi))$, which is given in Fig. 5 (c). While the tomographic reconstruction shows the superposition of all flame modulation effects, the field obtained from flame displacement $Re(q'_{\Delta}(\mathbf{x},\varphi))$ in Fig. 5 (c) decomposes only the effect of the individual mechanism on the flame modulation. A substraction of both fields $Re(q'_{\mathcal{R}}(\mathbf{x},\varphi) - q'_{\Delta}(\mathbf{x},\varphi))$ yields a remaining fluctuation quantity $Re(q'_{\rho}(\mathbf{x},\varphi))$, which is attributed to a coupling mechanism with the local acoustic density (inducing a local flame deformation). Ultimately, the decomposition of the flame modulation effects from experimental data can be compared to those obtained from numerical simulations. The latter fields are also taken from [2] and are shown in Fig. 5 (c). Especially the comparison of the decomposed fields indicates an accurate agreement of the experimental and numerical fields in a quantitative manner. For details on the local effects that can be observed from these results, see [1, 2, 3].

## 6. Conclusion

This paper presents an identification methodology of the acoustically induced flame displacement as observed in a lean-premixed gas turbine combustor experiment, exhibiting a high-frequency transverse instability. The evaluation of the displacement field relies on experimental pressure phase-conditioned OH$^\star$CL measurements, which are relatively simple to obtain compared to acoustic PIV measurements of the reactive flow. A robust evaluation of the displacement induced flame modulation is of interest for decomposition and analysis of the non-compact driving mechanisms observed in gas turbine thermoacoustics, to ultimately gain more insight into the physical behavior of such systems.

From the OH$^\star$CL recordings, a distinct motion of the flame with the acoustic gradient is observed, which confirms observations from previous works. The resulting displacement field is evaluated via pre-processing and cross-correlating the instantaneous flame images. A pressure-phase conditioned averaging of the resulting displacement fields yield the oscillatory displacement of the flame, from which the heat release modulations can be obtained. In order to assess the methods applicability, these fields are compared to synchronously obtained fields by PIV measurements and show good agreement.

With this method, the displacement effect throughout an oscillation cycle and its amplitude dependence is studied. Ultimately, the flame modulation mechanisms - namely displacement and density driving - are visualized in a decomposed manner and allow for further validation of analytic source term representations.

## Acknowledgments

The investigations were conducted as part of the joint research programme COOREFLEX-turbo in the frame of AG Turbo. The work was supported by the Bundesministerium für Wirtschaft und Technologie (BMWi) as per resolution of the German Federal Parliament under grant number 03ET7021T and the industry partner, which is gratefully acknowledged.

## REFERENCES

1. Berger, F. M., Hummel, T., Schuermans, B. and Sattelmayer, T. Pulsation-Amplitude-Dependent Flame Dynamics of High-Frequency Thermoacoustic Oscillations in Lean-Premixed Gas Turbine Combustors, *Proc. of the Asme Turbo Expo 2017*, Charlotte, NC, USA, (2017).
2. Berger, F. M., Hummel, T., Hertweck, M., Kaufmann, J., Schuermans, B. and Sattelmayer, T. High Frequency Thermoacoustic Modulation Mechanisms in Swirl Stabilized Gas Turbine Combustors - Part One: Experimental Investigation of Local Flame Response, *J ENG GAS TURB POWER*, **139**, (2017).
3. Hummel, T., Berger, F. M., Hertweck, M., Schuermans, B. and Sattelmayer, T. High-Frequency Thermoacoustic Modulation Mechanisms in Swirl-Stabilized Gas Turbine Combustors -Part Two: Modeling and Analysis, *J ENG GAS TURB POWER*, **139**, (2017).
4. Pfadler, S., Beyrau, F. and Leipertz, A. Flame front detection and characterization using conditioned particle image velocimetry (CPIV), *OPT EXPRESS*, **15** (12), (2007).
5. Fischer, A., Bake, F., Heinze, J., Diers, O., Willert, C. and Röhle, I. Off-line phase-averaged particle image velocimetry and OH chemiluminescence measurements using acoustic time series, *MEAS SCI TECHNOL*, **20** (7), 75403, (2009).
6. Sangl, J., Mayer, C. and Sattelmayer, T. Dynamic Adaptation of Aerodynamic Flame Stabilization of a Premix Swirl Burner to Fuel Reactivity Using Fuel Momentum, *J ENG GAS TURB POWER*, **133** (7), 071501, (2011).
7. Schwing, J., Sattelmayer, T. and Noiray, N. Interaction of Vortex Shedding and Transverse High-Frequency Pressure Oscillations in a Tubular Combustion Chamber, *Proc. of the ASME Turbo Expo 2011*, Vancouver, BC, Canada, (2011).
8. Westerweel, J. Fundamentals of Digital Particle Image Velocimetry, *MEAS SCI TECHNOL*, **8**, 1379–1392, (1997).
9. Thielicke, W. and Stamhuis, E. J. PIVlab - Towards User-friendly, Affordable and Accurate Digital Particle Image Velocimetry in MATLAB, *Journal of Open Research Software*, **2** (1), (2014).
10. Huang, H., Dabiri, D. and Gharib, M. On Errors of Digital Particle Image Velocimetry, *MEAS SCI TECHNOL*, **8** (897), pp. 1427–1440, (1997).